RSC Advances

PAPER

View Article Online
View Journal | View Issue

Open Access Article. Published on 06 November 2025. Downloaded on 5/22/2026 10:59:20 PM.
This article is licensed under a Creative Commons Attribution-NonCommercial 3.0 Unported Licence.

Check for updates

Cite this: *RSC Adv.*, 2025, **15**, 42931

Received 29th April 2025
Accepted 27th October 2025

DOI: 10.1039/d5ra03011k

rsc.li/rsc-advances

Investigating the applicability of HEPES–AuNPs for SERS measurements on individual functional red blood cells in saline

Cheviri Ghanashyam, †‡[a] Panchanil Sarmah, †[a] Anil Kumar Pal [b]
and Aseefhali Bankapur *[a]

Applying plasmonic metal nanoparticles (PMNPs) to perform surface-enhanced Raman spectroscopy (SERS) of live cells in physiological media, such as saline, has been challenging, as they generally aggregate in these media. However, PMNPs synthesized using physiological media, such as 4-(2-hydroxyethyl)-1-piperazineethanesulfonic acid (HEPES), are stable in saline. However, evaluating the role of HEPES–PMNPs in SERS of cell components is essential. This study uses near-infrared (NIR) vortex beam excitation to investigate the influence of PMNPs on the Raman spectra of cells in functional RBCs decorated with HEPES-reduced gold nanoparticles (AuNPs) in saline. The RBC spectra include contributions from membrane lipids, transmembrane proteins, and carbohydrate extensions. Higher plasmonic enhancements are seen in amide III bands at 1240, 1244, and 1268 cm^{-1}, a few amino acid frequencies, and CH_2 deformations at 1447 and 1455 cm^{-1} from proteins and lipids, respectively. Hemoglobin Raman peaks showed relatively less plasmonic enhancement. Furthermore, HEPES–AuNPs showed good stability in saline, and the FESEM and flow cytometry measurements on control and NPs-decorated RBCs confirmed the adherence of AuNPs on RBCs.

1. Introduction

For decades, optical trapping combined with Raman spectroscopic measurements has paved the way for probing single cells dispersed in physiological media, eradicating the adhesion-induced physical and chemical modifications in biological cells.[1] The technique has successfully delivered a comprehensive knowledge of cellular composition, behavior, and underlying biological processes by probing individual functional cells.[2–7] Although live-cell spectroscopy gained popularity in biomedical applications, studying metabolically active cell membranes remained a dream for many researchers. By adopting an optical vortex beam, we transcended the limitations of traditional methods, exploring the uncharted territory of membrane-targeted investigations in functional cells.[8] However, the intrinsically low Raman scattering cross-section has always limited the broader application in detecting disease-specific biomarkers in cells and organelles, including intact cell membranes. Further enhancing the membrane-bound Raman signals using plasmonic metal nanoparticles (PMNPs) will increase detection sensitivity, facilitating the identification of membrane-specific biomarkers. Although tip-enhanced Raman scattering (TERS) can play a crucial role in enhancing cell membrane features, it suffers from complex experimentation and a reduced probe area.

However, in biological applications, the biocompatibility of PMNPs is crucial, and studies have found that silver nanoparticles (AgNPs) can become cytotoxic by inducing cell cycle arrest, oxidative stress, chromosome aberrations, and DNA strand breaks.[9–11] In our previous study of the interaction of live RBCs with AgNPs, we observed changes in the heme conformation from an R to a T state owing to changes in intracellular pH. Intracellular pH changes arise due to the blockage of membrane transport function by the AgNPs.[12] The scientific literature on AuNP toxicity is controversial, and it is understood that gold nanoparticle (AuNP) cytotoxicity is multidimensional and depends on several factors, including the AuNP-cell combination, AuNP size and shape, AuNP dose and surface charge, as well as the cytotoxicity probing methods employed.[13] Moreover, AuNPs are the most efficient and extensively used substrates for biological applications owing to their increased signal enhancement factors under bio-friendly NIR excitations.

However, in biomedical applications, keeping AuNPs aggregate-free is also vital, as it has been reported that the stability of PMNPs drops drastically in physiological

---

[a] Manipal Institute of Applied Physics, Manipal Academy of Higher Education, Manipal 576104, Karnataka, India. E-mail: asif.bankapur@manipal.edu

[b] Department of Physics and Nanotechnology, College of Engineering and Technology, SRM Institute of Science and Technology, Kattankulathur, Chennai 603203, Tamil Nadu, India

† Both authors have contributed equally.

‡ Present Address: Department of Physics, Faculty of Engineering and Technology, JAIN (Deemed to be University), Bangalore, 562112, India.

© 2025 The Author(s). Published by the Royal Society of Chemistry

Open Access Article. Published on 06 November 2025. Downloaded on 5/22/2026 10:59:20 PM.
This article is licensed under a Creative Commons Attribution-NonCommercial 3.0 Unported Licence.

conditions.[14,15] Typically, physiological buffers (pH = 7.2–7.4) are employed in *in vitro* studies to maintain osmotic pressure and match essential electrolyte concentrations. However, NP dispersion in a physiological buffer medium leads to aggregation due to charge screening on the NP surface.[14] Meanwhile, 4-(2-hydroxyethyl)-1-piperazineethanesulfonic acid (HEPES), a zwitterionic buffer used in cell culture media with a pH range of 7.2–7.6, exhibits high solubility, membrane impermeability, chemical stability, and low absorbance in the UV-visible region, and has been utilized for AuNP synthesis. HEPES has been identified as a reducing, stabilizing, and shape-directing agent for the synthesis of Au nanostars *via* a seedless, surfactant-free procedure.[16,17] A study by Yuan *et al.* claims that the HEPES bilayer protects the AuNPs through sulfonate anchoring and hydrogen-bonded hydroxyl terminal groups.[18] Even incubation of AuNPs prepared using HEPES in PBS over six hours showed only a minimal loss of absorption coefficient in the UV-vis spectra.[19]

Regarding cell membrane studies, red blood cells (RBCs) are suitable models for examining membrane function, structure, and biological processes, as they lack subcellular components. In addition to acting as a passive barrier, the cell membrane performs various functions, such as cell signaling, cell adhesion, endocytosis, and exocytosis, and can also act as a receptor for foreign bodies like viruses.[20] Thus, studying cell membranes will provide a comprehensive understanding of their functions, compositions, and roles in disease progression and pathogenesis. Premasiri *et al.* reported SERS studies of RBCs on an Au substrate under 785 nm for the first time, but failed to identify the membrane contributions.[21] In previous studies of RBC membranes on Au substrates, the RBCs were either adhered to ref. 22 settled on the substrate, or converted to ghosts.[23] In this study, we have attempted to evaluate the influence of HEPES–AuNPs on the Raman signals emanating from vortex beam-trapped individual functional RBCs. Flow cytometry has been employed to assess the possible adverse effects of HEPES–AuNPs on RBCs.

2. Experimental methods

2.1. Chemicals

Gold(III) chloride trihydrate ($HAuCl_4 \cdot 3H_2O$), HEPES (≥99.5%), sodium chloride (NaCl), and sodium hydroxide (NaOH) were procured from Sigma-Aldrich.

2.2. AuNP synthesis and characterization

AuNPs were synthesized by following the protocol described by Liu *et al.*;[24] in brief, 6 mL of 50 mM HEPES solution was brought to a pH of 7.4 using 1 N NaOH solution. Next, 150 μL of 10 mM $HAuCl_4 \cdot 3H_2O$ was added and left for NP growth for 1 hour. The absorption spectra of AuNPs were obtained using a Jasco UV/visible spectrophotometer. The morphological characterization of prepared AuNPs was carried out using a high-resolution transmission electron microscope (HRTEM, JEM-2100Plus, Jeol, Japan). The hydrodynamic parameters, including particle size (*Z*-average), size distribution, and zeta potential, were measured using a DLS system (Zetasizer Pro, Malvern Instruments), which is equipped with a non-invasive backscatter (NIBS) optical design (detection angle: 173°). In DLS measurements, the *Z*-average is the intensity-weighted, harmonic-averaged particle diameter, calculated using the well-documented cumulant method.[25]

2.3. Sample preparation

Freshly drawn blood from a healthy volunteer was incubated with and without AuNPs at 37 °C and 5% CO_2 for 6 hours. The incubated blood was then diluted with 1.5 mL of isotonic NaCl, and the resulting suspension was immediately used for Raman spectroscopy and flow cytometry experiments. For Raman measurements, about 200 μL of RBC suspension was dropped on a quartz coverslip placed in the microscope sample plane. Individual RBCs were optically levitated a few microns above the coverslip using the donut focal spot of the vortex beam in a face-on orientation to collect the scattered radiation efficiently. For FESEM imaging, the RBC suspensions were drop-casted on top of a stainless steel substrate and allowed to dry at room temperature overnight. The prepared sample was subjected to FESEM imaging the next day.

2.4. Optical setup

We utilized a laboratory-built single vortex-beam optical tweezers setup for membrane-targeted Raman measurements. The schematic representation of the setup is shown in Fig. 1. It uses a modified dual-objective upright microscope with an inverted configuration for stable optical trapping of cells. A 785 nm diode laser (Ondax, USA) with a maximum output power of 175 mW, spectral linewidth of 124 pm, output beam diameter of 2.7 mm, and a nearly Gaussian intensity profile (TEM_{00}) was used as an excitation source. The laser beam was expanded using a 4× beam expander, comprised of a plano-concave lens ($f = 2.5$ cm) and a biconvex lens ($f = 10$ cm).

A spiral phase plate (Holo/or, Israel) with a topological charge, $m = 12$, placed in the beam path induces a spiral wavefront in it to form an optical vortex, which, when focused using the lower 40×, 0.75 NA objective (OB1), produces a donut-shaped focal spot (as shown in Fig. 2a). The donut focal spot size is adjusted to match the RBC diameter (6–8 μm) to facilitate simultaneous trapping and Raman excitation of individual functional RBCs suspended in the physiological buffer (NaCl). The upper 60×, 1.0 NA water immersion objective (OB2) collects the scattered signal from the membrane of the RBC trapped in face-on orientation. The sample plane of the microscope was imaged using a CMOS camera (DSFi3, Nikon, Japan).

After filtering out the Rayleigh scattered light with an optical edge filter, the collected signal is fed into the spectrograph using an *f*/4 lens (Semrock, USA). The Raman signals were dispersed using the Horiba Jobin Yvon *i*HR320 spectrograph, which has a 1200 grooves per mm grating blazed at 750 nm. Signal detection is performed by a liquid nitrogen-cooled charge-coupled detector (Symphony II CCD-1024 × 256) operating at 140 K. All Raman acquisitions are performed at a laboratory temperature of 22 °C, with a CCD acquisition time of 60 seconds and 2 average accumulations.

© 2025 The Author(s). Published by the Royal Society of Chemistry

Open Access Article. Published on 06 November 2025. Downloaded on 5/22/2026 10:59:20 PM.
This article is licensed under a Creative Commons Attribution-NonCommercial 3.0 Unported Licence.

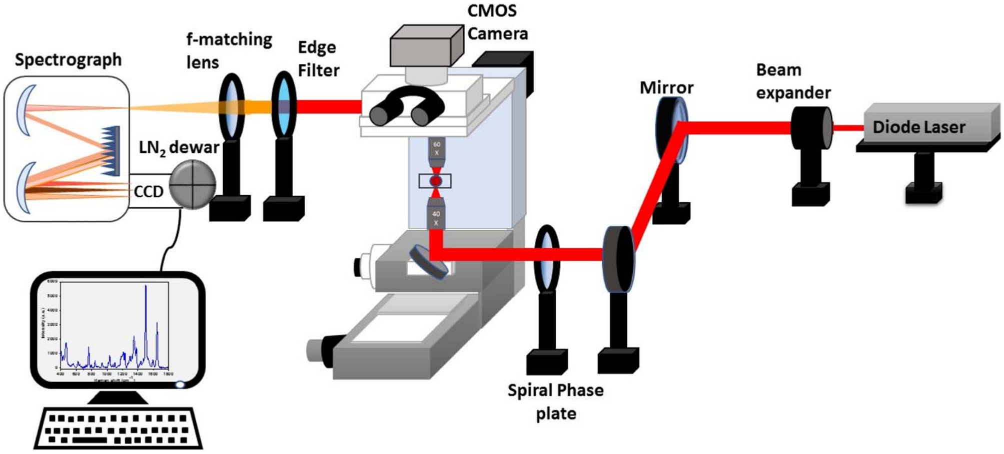

Fig. 1 Schematic of the experimental setup for membrane-targeted Raman measurements on an optically trapped individual functional RBC.

2.5. RBC trapping using an optical vortex beam

Fig. 2a depicts the conversion of the laser beam spot from a Gaussian profile to a doughnut profile upon passing through an SPP. The doughnut spot is characterized by a central null region with an intensity gradient in its annular part. Fig. 2b and c show the transverse intensity distribution for Gaussian and vortex beams profiled at the focal spot of a 30 cm biconvex lens using the slit-scanning method.

Single, live RBCs with and without AuNP decoration were trapped using a vortex beam in face-on orientation, as shown in Fig. 2e and d shows the edge-on orientation of RBCs in conventional Gaussian beam trapping for comparison. For stable single-beam optical trapping, the optical forces must produce a three-dimensional equilibrium wherein there is a delicate balance between transverse and longitudinal gradient forces to counter the unidirectional scattering force. In conventional optical trapping using a Gaussian beam, tight focusing with a high NA objective creates the longitudinal intensity gradient. In contrast, the transverse intensity gradient is intrinsic to the Gaussian profile. In the case of vortex beam trapping, a transverse intensity gradient exists throughout the bright annular region, and a longitudinal gradient at the rim can be created by focusing the beam with high-NA objectives. The vortex beam trapping requires that the inner diameter of its focused spot be marginally less than the cell diameter so that the bright central part of the annular spot holds the cell membrane. Hence, the beam also excites a thin layer of hemoglobin (Hb) near the membrane. The supplementary video shows that the RBC is stably held by its edges, maintaining its face-on orientation.

3. Results and discussions

3.1. AuNP characteristics and stability in saline

We evaluated the stability of HEPES–AuNPs in saline by keeping the NP suspension in saline for 6 hours and then subjecting it to UV-vis spectrophotometry at various time intervals. The point-baseline UV-vis spectra of prepared AuNPs show the plasmonic absorption peak at 653 nm and another peak at 340 nm with a shoulder at 377 nm, possibly due to ligand–metal transitions or from spherical AuNPs of very small size (<2 nm).[26] Fig. 3a and b compare the absorption spectra of as-prepared AuNPs and AuNPs in saline monitored over 6 hours. The 653 nm peak showed a decrease in intensity only when in saline, and the 340 nm peak showed an increase in intensity only in as-prepared AuNPs. Additionally, the 377 nm shoulder in as-prepared AuNPs blue-shifted to 372 nm after 3 hours of adding saline and exhibited an increase in intensity. Notably, the increase in 372 nm peak intensity is concomitant with a decrease in the 653 nm peak intensity. This may be due to halide ion-induced etching, resulting in the formation of small spherical AuNPs,[27,28] as evident from the TEM image in Fig. 3f. However, we have not observed any aggregation of AuNPs when adding saline for over 6 hours, as the plasmonic peak remains near 653 nm and no secondary absorption beyond that. The increase in intensity of the 340 nm peak indicates that the formation of more metal–ligand complexes/spherical AuNPs occurs with time, which ceases on the addition of saline.

Fig. 3c and d show the size distribution measured by the DLS, with insets showing the cumulants fit for three trials. The *Z*-average was calculated to be 29.73 ± 3.63 nm for HEPES AuNPs and 32.54 ± 4.13 nm for HEPES AuNPs in saline, indicating that nanoparticles are quite stable in saline without a visible increase in size. However, the intensity distribution shows a slight broadening near 160 nm, suggesting that a few AuNPs displayed an increase in hydrodynamic diameter. Thus, there might be a slight aggregation that was not that apparent in the UV-vis spectrum. The presence of a plasmonic peak at 653 nm and the absence of new peaks in UV-vis spectra and an insignificant increase in average particle size in DLS measurements after saline treatment indicate that most of the HEPES–AuNPs are stable in saline and do not form aggregates. The zeta potential measurements are performed on as-prepared and saline-treated AuNPs, and the results are shown in Fig. S1. The zetapotential value increased from −37 mV to −27 mV after saline treatment due to charge screening, but this did not lead to aggregation.

Open Access Article. Published on 06 November 2025. Downloaded on 5/22/2026 10:59:20 PM.
This article is licensed under a Creative Commons Attribution-NonCommercial 3.0 Unported Licence.

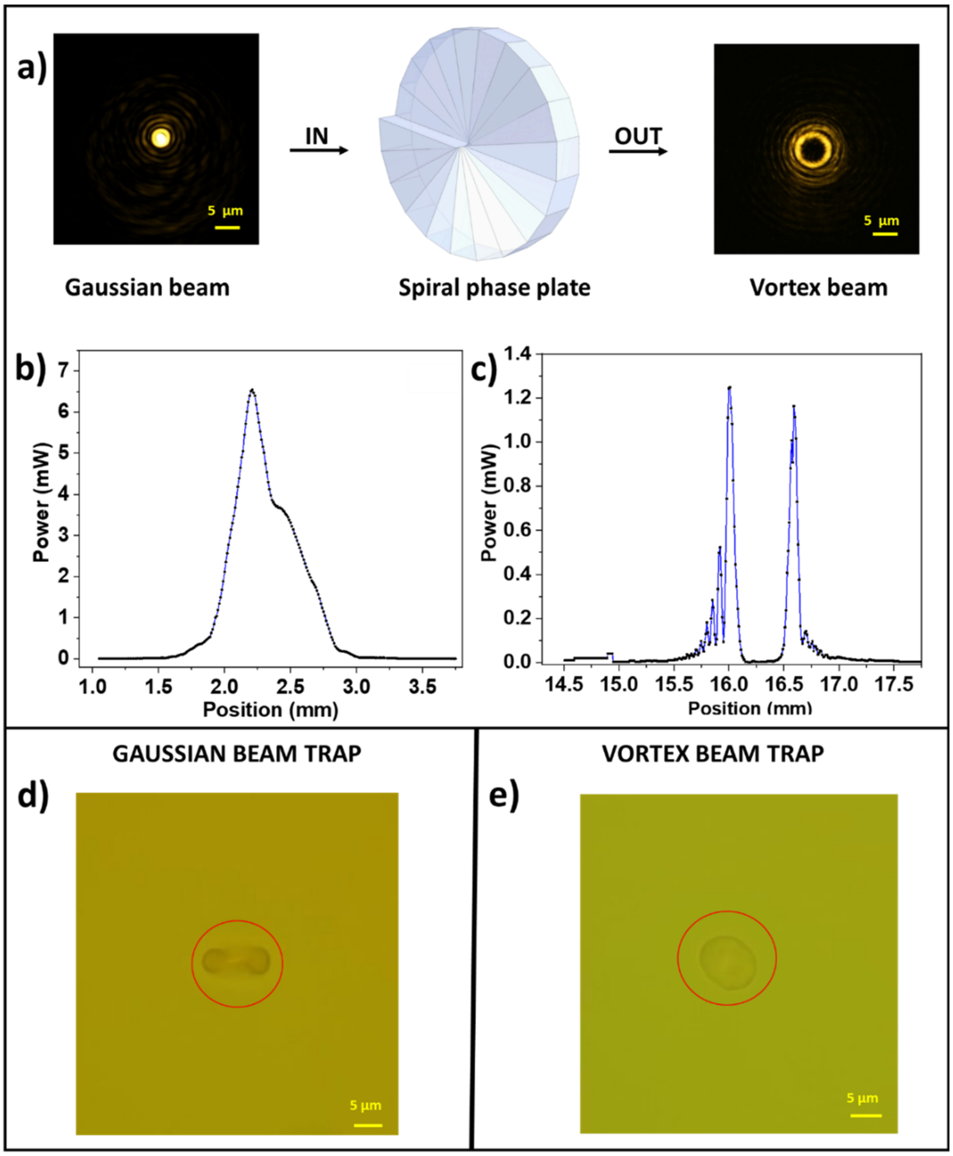

Fig. 2 (a) Conversion of Gaussian to vortex beam using SPP. The transverse beam profile of (b) the Gaussian and (c) the vortex laser beam. Optical image of live single RBC trapped using (d) Gaussian beam and (e) vortex beam.

The TEM imaging revealed the exact morphology of the AuNPs before and after saline treatment, as shown in Fig. 3e and f. The prepared AuNPs are nanostars with a diameter of approximately 30 nm, as measured from tip to tip. Usually, spherical AuNPs of this size range have a plasmonic absorption peak around 520 nm. The large red shift in the plasmonic absorption peak of HEPES–AuNPs to 653 nm is due to their peculiar shape.[24]

3.2. AuNPs decorated RBCs: confirmation using flow cytometry and FESEM

The RBC membrane surface has a negative charge due to sialic acid-rich glycoproteins, which prevent RBCs from interacting with each other. Electronegative RBC membrane tends to adsorb positively charged and neutral particles. The NPs can adsorb on the RBC surface *via* van der Waals, steric, and/or electrostatic forces.[29] The NPs with hydrophilic capping agents are observed to interact with the cell surface *via* hydrogen bonding with peptide units.[30] Typically, NP internalization by cells occurs *via* endocytosis. For cells lacking endocytosis machinery, such as RBCs, internalization *via* passive transport remains the only option. However, the possibility of such internalization through the membrane channel following NP binding is minimal and is highly dependent on the NP size.[6,22] As the cell membrane pores are about 2.2–2.4 nm in size[31] and as the prepared nanoparticles are larger, their internalization through non-facilitated diffusion is not possible. Hence, the AuNPs capped with HEPES are expected to decorate the RBC membrane upon incubation, possibly through hydrophilic interactions with the peptide units of transmembrane proteins. Moreover, since HEPES is not a membrane-active agent, its membrane impermeability reduces the probability of any other facilitated internalization of the NPs.

Open Access Article. Published on 06 November 2025. Downloaded on 5/22/2026 10:59:20 PM.
This article is licensed under a Creative Commons Attribution-NonCommercial 3.0 Unported Licence.

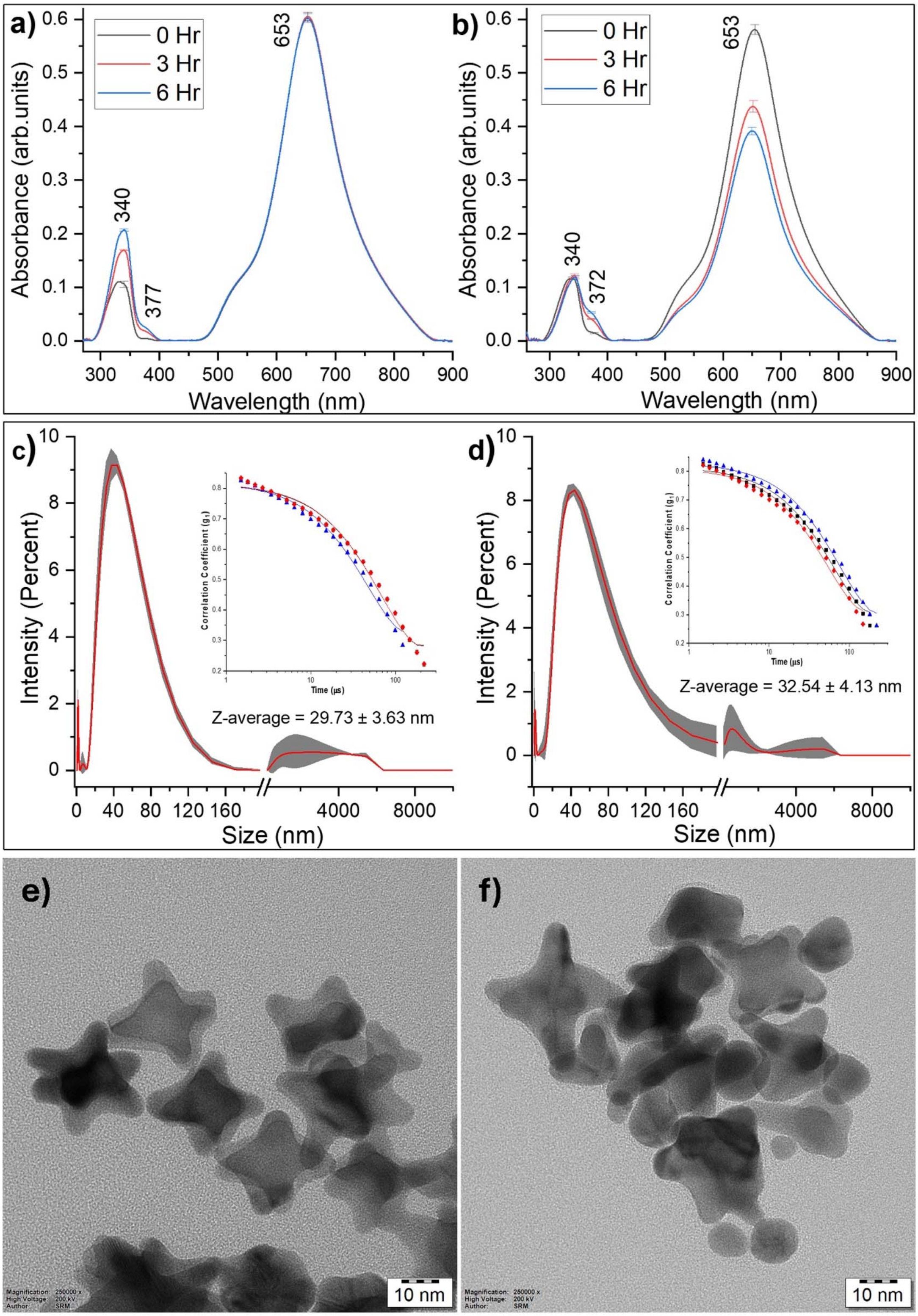

Fig. 3 Stability of AuNPs in saline using UV-vis and DLS measurements for as-prepared AuNPs (a and c) and AuNPs in saline (b and d). The insets in (c) and (d) show the cumulants fit for three trials. The TEM images of (e) as-prepared and (f) saline-treated AuNPs.

Flow cytometry is an advanced method for assessing and classifying cell populations based on various physical attributes of individual cells, such as size and granularity, as the cells move through a measuring device while suspended in a fluid. The functionality of this instrument relies on the light-scattering properties exhibited by the cells being analyzed. Upon laser interaction with the cell, two types of light scattering occur: forward scatter (FSC) and side scatter (SSC). FSC results

Open Access Article. Published on 06 November 2025. Downloaded on 5/22/2026 10:59:20 PM.
This article is licensed under a Creative Commons Attribution-NonCommercial 3.0 Unported Licence.

from light diffraction collected along the laser beam axis, whereas SSC measures light scattering at a ninety-degree angle relative to the laser. Cell size, granularity, shape, and surface topography influence the total light scattering. FSC is proportional to the cell surface area or size, and SSC primarily measures the refracted and reflected light corresponding to cell granularity or internal complexity.[32]

The adherence of AuNPs on the surface of RBCs can be conceptualized as the introduction of granularity to the RBC surface. Therefore, we hypothesized that the cell granularity, as measured by side scatter (SSC) in flow cytometry, could be a reliable indicator to confirm the presence of AuNPs on the RBC surface. Fig. S2 shows the FSC-H *vs.* SSC-H plots for fresh and incubated control RBCs and RBCs incubated along with AuNPs, respectively. A significant rise in SSC intensity for AuNP-incubated RBCs compared to those of control RBCs suggests that the NP decoration has been achieved in the former case. Additionally, there is an observable augmentation in forward scattering for NP-decorated RBCs, as shown in Fig. S2c. Fig. S2a and b illustrate that both fresh control RBCs and those subjected to a 6-hour incubation period display a population characterized by low SSC-H values. Moreover, they exhibit comparable FSC-H values, indicating that the cells remain intact throughout the incubation period. The single histogram SSC and FSC plots in Fig. 4a and b show a shift of ~90% and ~63%, respectively, for AuNP-incubated RBCs compared to control classes, indicating increased granularity and slightly larger size in the former cells. We have also performed field-emission scanning electron microscopy (Apreo S FESEM, ThermoScientific, USA) imaging of control and AuNP-decorated RBCs, and the images are shown in Fig. 4c and d for control and Fig. 4e and f for AuNP-decorated RBCs at two different magnifications. The bright spots in FESEM images clearly indicate the presence of AuNPs in the membrane. The AuNPs imaged on the RBC surface lack contrast due to charging effects, which is not the case when imaged on conducting substrates. The flow cytometry and FESEM results underscore the confirmation of AuNPs' adherence to the surface of RBCs.

3.3. Membrane-targeted Raman measurements of single, functional RBCs

Raman measurements of individual functional RBCs with and without HEPES–AuNPs decoration were carried out using a vortex beam trapping setup. Fig. 5 compares the Raman spectra of RBCs with and without HEPES–AuNP decoration obtained at an excitation power density of $\sim 9.8 \times 10^4$ W cm^{-2} and for an acquisition time of 60 s with 2 average accumulations. Such low excitation power density circumvents any issues arising from photochemical and photothermal effects in the spectrum.[33] The intensity of Raman spectra is normalized with respect to that of the 791 cm^{-1} band arising from the coverslip. The single-cell Raman spectra express contributions from Hb, proteins, lipids, and carbohydrates. On comparing the Raman spectra (Fig. 5) of RBCs with and without AuNPs, we observed that the Raman peaks have varying amounts of signal enhancement in the RBCs with AuNPs. We also observed frequency shifts in certain Raman peaks in AuNP-incubated RBC spectra compared to Raman spectra without AuNPs, possibly due to changes in the molecular environment resulting from the presence of AuNPs. For easier comparison, the Raman spectra are divided into three regions (Region I: 550–1015 cm^{-1}, Region II: 1016–1424 cm^{-1}, Region III: 1425–1750 cm^{-1}) and presented in Fig. 5. The observed changes in each cell component are explained below. However, for clarity, the entire spectrum, along with the control spectrum of HEPES–AuNP in saline, is compared in Fig. S3.

3.3.1. Contributions from protein and amino acid residues. AuNP-decorated RBC spectra show enhancement in signals from various amino acid residues, such as tryptophan, phenylalanine, tyrosine, lysine, histidine, and glutamic acid, and bands from sulfur-containing amino acid residues cysteine and methionine. As evident from the spectra, signals corresponding to aromatic amino acids show considerable enhancement. The Raman frequency assignments for the spectral features in Fig. 5 were performed using previous literature, and the results are summarized in Table S1. The bands assigned to indole ring stretching vibrations in tryptophan appear at 884, 1259, 1553, and 1577 cm^{-1}. The 1332 cm^{-1} band, corresponding to C_β rock, appears to be the most enhanced tryptophan band. The C–C stretching modes of phenylalanine observed at 1000 and 1337 cm^{-1} exhibit increased intensity. The C–H out-of-plane bending in phenylalanine appears at 744 cm^{-1} as a shoulder peak but is enhanced. The enhanced 1604 cm^{-1} band is usually assigned to ν_{19} in heme but can also originate from the C–C stretching in phenylalanine. C–H out-of-plane bending in tyrosine is solely observed in AuNPs decorated membrane spectra at 847 cm^{-1}, whereas the enhanced peaks corresponding to ring stretching appear at 1268 and 1619 cm^{-1}, of which 1268 cm^{-1} originates from C–O vibration.

In the case of sulfur-containing amino acids such as cysteine and methionine, the C–S stretching vibrations are expressed at 652, 676, and 698 cm^{-1}, respectively. Amino acids featuring charged side chains, such as lysine, histidine, arginine, and glutamic acid, display increased intensity in the AuNPs decorated membrane spectra. Similarly, amino acids such as alanine, proline, and isoleucine also appeared to be enhanced in the AuNP-decorated membrane spectra. The lysine contributes to 847 and 1291 cm^{-1} peaks corresponding to the lysyl side-chain deformations. A relatively strong band at 1268 and 1480 cm^{-1} can be assigned to the in-plane C–H bending of imidazole and ring stretching of histidine, respectively. Another contribution from histidine is observed at 1358 cm^{-1}, attributed to C–H bending. The contribution from the aliphatic side chains of arginine is observed at 1291 cm^{-1}, originating from its long-chain deformation. The deformations in the carboxyl group of glutamic acid are seen at 931 cm^{-1}, whereas the CH$_2$ deformation is observed at 1309 cm^{-1}. Different vibrations in proline, isoleucine, and alanine also appear in the AuNPs decorated membrane spectra at 987, 918, and 1358 cm^{-1}, respectively.

Vibrational contribution from the protein backbone peaks, including CH/CH$_2$ deformations, amide bands, *etc*, and aromatic amino acid side chains in proteins, is prominent in

© 2025 The Author(s). Published by the Royal Society of Chemistry

Open Access Article. Published on 06 November 2025. Downloaded on 5/22/2026 10:59:20 PM.
This article is licensed under a Creative Commons Attribution-NonCommercial 3.0 Unported Licence.

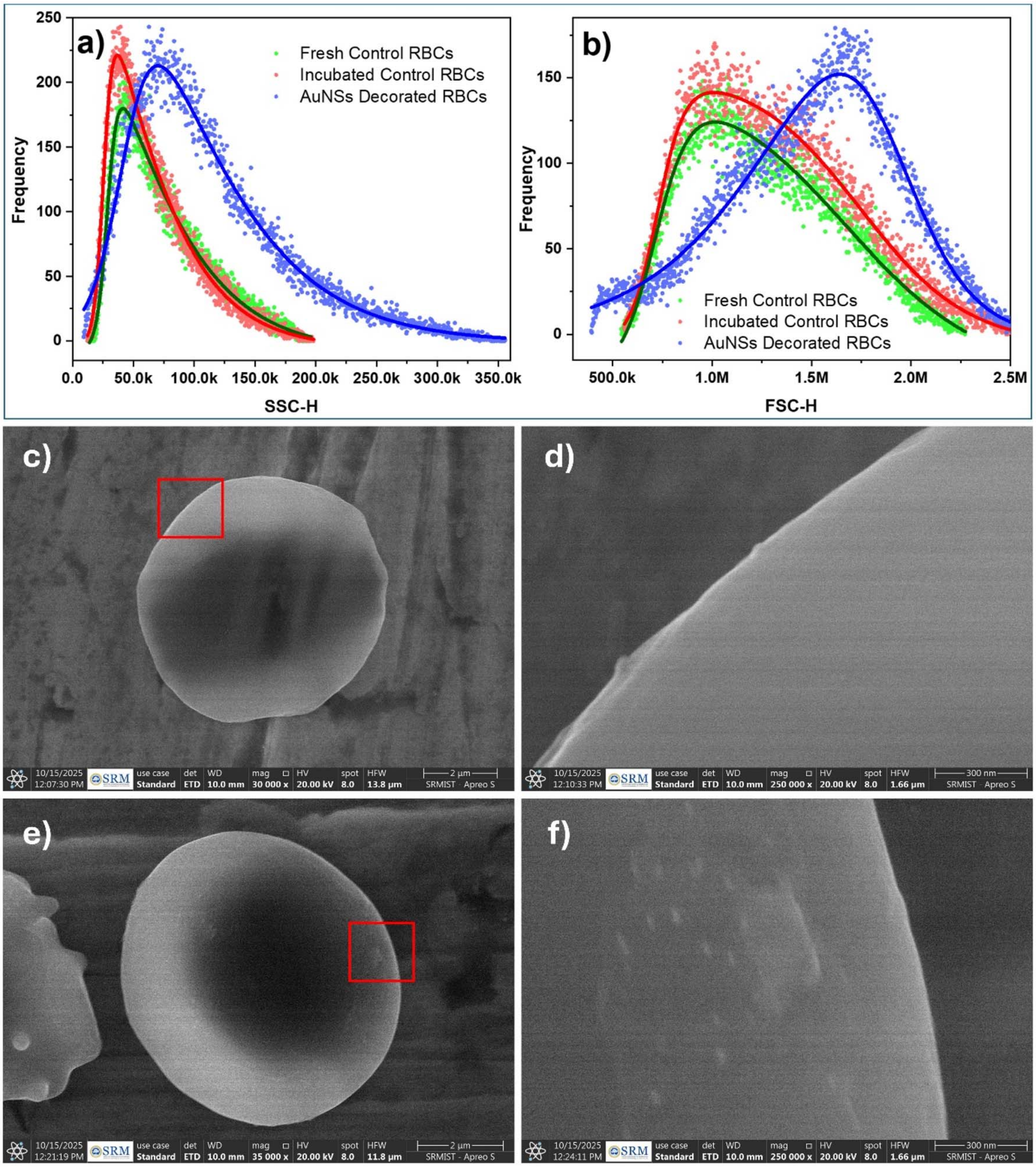

Fig. 4 Flow cytometry results showing the shift in (a) SSC-H and (b) FSC-H peak frequencies for RBCs upon AuNPs decoration. FESEM images showing the control RBCs (c and d) and RBCs upon AuNPs decoration (e and f).

the AuNPs decorated membrane spectra, with amide III bands showing the maximum enhancement. Table 1 shows the enhancement factors for various Raman frequencies calculated using background-subtracted Raman and SERS spectra (Fig. S4). The enhancement factors are calculated by dividing the peak intensity values of SERS spectra by those in conventional Raman spectra. The amide III bands, appearing at 1240 and 1244 cm^{-1}, corresponding to β-sheet and irregular structures of proteins, are intense in the AuNP-decorated membrane spectra, with an enhancement of ~6.7 and 6. The peak due to the helical structure of amide III is also strongly enhanced by a factor of 6 and positioned at 1268 cm^{-1}. The amide I band at 1653 and 1662 cm^{-1}, assigned to α-helices in protein secondary structure, appears to be less enhanced with a factor of ~3.5 and is expected to arise from Hb as it is mainly comprised of α-helices. The intense 1637 cm^{-1} peak can be assigned to Amide I (β-sheet), but in RBCs, it is conventionally assigned to $\nu_{\mathrm{as}}(C_{\alpha}C_{m})$ of the heme molecule in Hb, and it is also enhanced by a factor of 3.3. The CH$_2$ deformation band of protein side chains at 1447 cm^{-1} is intense in the AuNP-decorated membrane spectra, showing an enhancement by ~4 times. The peaks attributed to the protein disulfide bridge –C–S–S–C– appear at 670 and 674 cm^{-1} for C–S stretching. The band at 896 cm^{-1} can be assigned to the skeletal C–C stretching, and the N–C–C

Open Access Article. Published on 06 November 2025. Downloaded on 5/22/2026 10:59:20 PM.
This article is licensed under a Creative Commons Attribution-NonCommercial 3.0 Unported Licence.

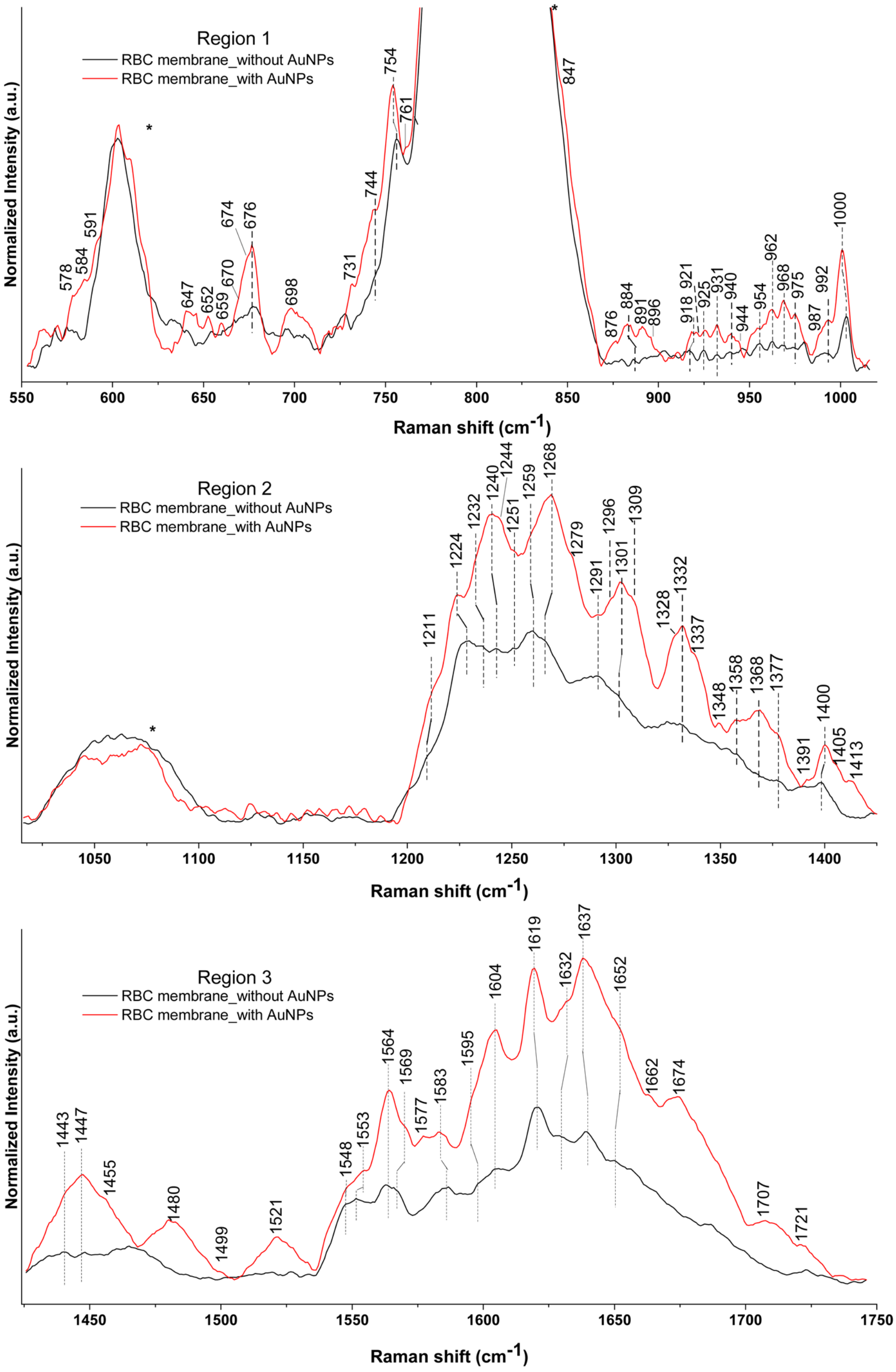

Fig. 5 Comparison of the Raman spectrum of the RBC membrane with and without HEPES–AuNPs of an optically trapped single live RBC membrane recorded using a vortex beam. Spectrum is divided into three regions for ease of analysis. Region I: 550–1015 cm^{-1}, Region II: 1016–1424 cm^{-1}, Region III: 1425–1750 cm^{-1}.

stretching can be located at 925 and 931 cm^{-1}. The side chain C–H deformation frequency is located at 1309 cm^{-1} and is intense in the AuNP-decorated membrane spectra with a 6.7-fold amplification.

The selective enhancement is due to the vicinity of AuNPs to the protein backbone and extended side chain moieties like –CH/–CH$_2$ groups, aromatic rings, and imidazole ring. Fazio *et al.*[30] observed similar SERS enhancements in phenylealanine and BSA when treated with NPs and predicted that a potential cause for such enhancements is due to the interactions of exposed peptide units with hydrophilic surfaces *via* hydrogen bonding. Another possible interaction can be through nano-invaginations of the RBC membrane by the AuNPs, as observed by Brazhe *et al.*[29] This is possible due to the small size of the HEPES AuNPs (~30 nm), which facilitates their penetration deeper into the membrane invaginations.

© 2025 The Author(s). Published by the Royal Society of Chemistry

Open Access Article. Published on 06 November 2025. Downloaded on 5/22/2026 10:59:20 PM.
This article is licensed under a Creative Commons Attribution-NonCommercial 3.0 Unported Licence.

Table 1 Estimated enhancement factors observed for various Raman frequencies

Sl. No.	Raman frequency (cm^{-1})	Enhancement	Sl. No.	Raman frequency (cm^{-1})	Enhancement
1	652	3.21	21	1268	6.03
2	670	[a]	22	1291	[a]
3	674	[a]	23	1309	6.70
4	676	2.47	24	1332	5.39
5	698	3.05	25	1337	3.82
6	731	[b]	26	1358	2.85
7	744	1.92	27	1447	3.99
8	847	2.26	28	1455	2.63
9	876	4.69	29	1480	4.95
10	884	[b]	30	1548	1.11
11	896	[b]	31	1553	[a]
12	918	2.30	32	1564	2.20
13	925	4.12	33	1577	2.81
14	931	[b]	34	1604	3.43
15	1000	1.78	35	1619	2.46
16	1211	3.47	36	1632	[a]
17	1224	1.44	37	1637	3.35
18	1240	6.70	38	1653	3.68
19	1244	6.07	39	1662	3.52
20	1259	[a]	40	1674	4.31

[a] Shoulder peak SERS spectrum. [b] Raman peak missing.

3.3.2. Contributions from lipids. RBC membrane is constituted by three kinds of lipids: phospholipids, glycolipids, and cholesterol, of which phospholipids are the main contributors.[34] Phosphatidylcholine (PC), phosphatidylserine (PS), phosphatidylethanolamine (PE), phosphatidylinositol (PI), and sphingomyelin (SM) are the main phospholipids present in the cell membrane. We observed several peaks attributed to different phospholipid vibrations, either enhanced or appearing only in the spectra of the AuNP-decorated membrane. Enhanced bands corresponding to backbone and acyl chains of various phospholipids appear at 1268 and 1455 cm^{-1} in the AuNPs decorated membrane spectra, whereas the 1296 cm^{-1} peak appears only in the AuNPs decorated membrane spectra. The C–N symmetric and antisymmetric stretching in the serine of PC and PS residues were observed at 731 and 876 cm^{-1}, respectively.

3.3.3. Contributions from carbohydrates. Different combinations of D-galactose, D-mannose, D-glucose, L-fucose, *N*-acetyl-D-glucosamine, rhamnose, and sialic acid constitute the oligosaccharide chains of membrane glycoproteins and glycolipids. However, the amount and proportion of these sugars vary greatly from one glycoprotein/glycolipid to another.[35] Thus, the peaks in the RBC membrane spectra can also have little contribution from carbohydrate molecules. The C–C/C–O stretching in carbohydrates can be observed in the 800–1200 cm^{-1} range, and CH/CH_2 deformations appear in the 1200–1500 cm^{-1} range. The vibrations in *N*-acetylneuraminic acid are expressed at 647, 847, 884, 896, 944, 1259, 1377, 1455, and 1663 cm^{-1}. The contribution from galactose in the spectra can be observed at 659, 891, 1244, 1309, 1332, and 1377 cm^{-1}. The bands at 884, 931, 1268, and 1455 cm^{-1} can be attributed to the vibrations from the mannose. The vibrations from fucose appear at 670, 876, 1259, 1332, and 1447 cm^{-1}. The contributions from *N*-acetyl-D-glucosamine were located at 931, 1259, and 1553 cm^{-1}, and those from D-(C)-galactosamine at 1268 cm^{-1}.

3.3.4. Contributions from Hb. Our previous work shows that most Hb molecules near the cell membrane are in an oxy state, while those within the cell are in a mixture of oxy and deoxy states. These results indicated a gradient in oxy-Hb concentration inside RBC, with its maximum close to the cell membrane. It is possible because oxygen is readily accessible close to the cell membrane, and diffusion-induced retardation causes oxygen concentration to decline away from the cell membrane.[8] Consistent with the previous study, the vortex beam excited Raman spectra contain signatures from the oxy state of Hb. However, with a slight increase in 1211 cm^{-1} peak intensity, the AuNPs-decorated membrane spectra show a few Hb molecules in the deoxy state. This is expected because the AuNPs decoration on the RBC membrane blocks the membrane transport channel, reducing Hb's oxygen-binding affinity.[6] The methine C–H deformation peak of the oxy-Hb molecules is at 1224 cm^{-1}, while that of the deoxygenated molecules is at 1211 cm^{-1}. When both oxy-Hb and deoxy-Hb molecules are present in the excitation focal volume, both peaks are seen in the resultant spectrum, and their relative intensity variations correspond to the variations in oxy-Hb to deoxy-Hb concentration. In the deoxy state of Hb, the conformational change brings the methine group close to the protein subunits, changing the C–H deformation angle and resulting in a frequency shift from 1224 cm^{-1} to 1211 cm^{-1}.[6] We observe a decrease in the 1224/1211 intensity ratio in the RBC membrane spectra without AuNPs compared to one with AuNPs, indicating a change in the Hb state. However, the spin state marker region (1520–1640 cm^{-1}) in the AuNP-decorated membrane spectra continues to represent the oxy state of Hb,

Open Access Article. Published on 06 November 2025. Downloaded on 5/22/2026 10:59:20 PM.
This article is licensed under a Creative Commons Attribution-NonCommercial 3.0 Unported Licence.

as these peaks are relatively less sensitive to the oxy-deoxy transformation. Upon comparing the two spectra, we observed that the Hb peaks are relatively less enhanced than the other bands. In the 1200–1400 cm^{-1} region, band 1224 cm^{-1} assigned exclusively to ν_{13} in Hb is dominant in the RBC membrane spectra without AuNPs, whereas it is the least enhanced peak in the region. We can also observe a similar trend in the spin state marker region, where bands such as 1548, 1583, and 1632 cm^{-1} assigned to Hb vibrations are minimally enhanced. The bands at 1604 and 1619 cm^{-1}, assigned to C=C vinyl stretching in Hb, appear to be enhanced; however, they also have contributions from stretching vibrations in phenylalanine and tyrosine, respectively, which are part of the membrane and hence prone to plasmonic enhancement. This trend is expected in the Raman spectra of AuNP-decorated RBCs, as the NPs are located on the cell surface, and hence in the vicinity of membrane components, but far from intracellular Hb molecules, leading to plasmonic enhancement only in the former case. However, the non-enhanced excitation field of the vortex beam reaches the Hb molecules, producing the Raman contribution from them.

4. Conclusions

Studying the interactions of cells suspended in physiological buffers, such as saline, with PMNPs is a challenge due to the stability of PMNPs in physiological conditions.[14,15] This study demonstrates that HEPES-capped AuNPs exhibit improved stability in saline. This has enabled Raman measurements of live RBC membranes decorated with AuNPs in saline using a vortex beam. The Raman spectra of the RBC membrane showed enhancement (~2–7 times) in the presence of AuNPs, indicating a possible occurrence of surface-enhanced Raman scattering. In conclusion, our study demonstrates the effectiveness of utilizing biocompatible HEPES–AuNPs decorated on RBCs in conjunction with vortex beam-based Raman tweezers to enhance the detection of membrane-specific vibrational contributions. Vortex beam-based optical tweezers can stably trap AuNP-decorated RBCs in an unconventional face-on orientation, enabling precise plasmonic excitation of their membrane components and overcoming the limitations posed by conventional Gaussian-based optical tweezers, which primarily collect signals from the bulk of the cell. Furthermore, flow cytometry and FESEM measurements confirmed the adherence of AuNPs to RBCs. The study provided enhanced membrane-specific vibrational signals attributed to proteins, lipids, and carbohydrates, leading to a more comprehensive understanding of the biochemical composition of RBC membranes. Our results are promising, and we look forward to further optimizing the conditions to study cell membrane modifications and the role of cell membranes in disease progression, pathogenesis, and the development of effective therapeutics. However, such a study requires acquiring SERS spectra from a large number of RBCs, which is beyond the scope of this work. This framework also holds promise for exploring other types of biological cells and membranes, potentially leading to advancements in biomedicine, pharmacology, and biotechnology.

Ethical statement

Ethical clearance was obtained from the Institutional Ethics Committee of Kasturba Medical College and Kasturba Hospital (Reg. No ECR/146/Inst/KA/2013/RR-19), approved on 01/10/2021 under Ref. No. IEC: 485/2021. The experiments were performed in compliance with the existing norms of the ethics committee. Informed consent was obtained from the concerned individual.

Conflicts of interest

The authors declare no conflict of interest.

Data availability

All data are included in the manuscript and supplementary information (SI) file. Supplementary information is available. See DOI: **https://doi.org/10.1039/d5ra03011k**.

Acknowledgements

The authors acknowledge the financial support from the Science and Engineering Research Board (SERB), Govt of India, under the CRG/2019/004088 grant for the experimental facility. C. Ghanashyam and P. Sarmah acknowledge the receipt of the TMA Pai PhD fellowship from the Manipal Academy of Higher Education. We acknowledge the Manipal Centre for Biotherapeutics Research (MCBR) of MAHE, Manipal, for helping with flow cytometry measurements. We acknowledge the SRM Central Instrumentation Facility (SCIF) at SRMIST for the FESEM and HRTEM facilities funded by the Ministry of New and Renewable Energy (MNRE).

References

1 J. W. Chan, D. S. Taylor and D. L. Thompson, The effect of cell fixation on the discrimination of normal and leukemia cells with laser tweezers Raman spectroscopy, *Biopolymers*, 2009, **91**, 132–139.

2 K. B. Soysal, S. Parlatan, M. Mastanzade, M. Ozbalak, M. N. Yenerel, M. B. Unlu, *et al.*, Raman tweezers as an alternative diagnostic tool for paroxysmal nocturnal hemoglobinuria, *Anal. Methods*, 2021, **13**, 3963–3969.

3 J. Dybas, F. C. Alcicek, A. Wajda, M. Kaczmarska, A. Zimna, K. Bulat, *et al.*, Trends in biomedical analysis of red blood cells – Raman spectroscopy against other spectroscopic, microscopic and classical techniques, *TrAC Trends in Anal. Chem.*, 2022, **146**, 116481.

4 A. C. De Luca, G. Rusciano, R. Ciancia, V. Martinelli, G. Pesce, B. Rotoli, *et al.*, Spectroscopical and mechanical characterization of normal and thalassemic red blood cells by Raman tweezers, *Opt. Express*, 2008, **16**, 7943–7957.

5 R. Liu, Z. Mao, D. L. Matthews, C.-S. Li, J. W. Chan and N. Satake, Novel single-cell functional analysis of red blood cells using laser tweezers Raman spectroscopy: Application for sickle cell disease, *Exp. Hematol.*, 2013, **41**(07/01/2013), 656–661.e1.

© 2025 The Author(s). Published by the Royal Society of Chemistry

Open Access Article. Published on 06 November 2025. Downloaded on 5/22/2026 10:59:20 PM. This article is licensed under a Creative Commons Attribution-NonCommercial 3.0 Unported Licence.

6 A. Bankapur, S. Barkur, S. Chidangil and D. Mathur, A micro-Raman study of live, single red blood cells (RBCs) treated with $AgNO_3$ nanoparticles, *PloS One*, 2014, **9**, e103493.

7 A. Bankapur, E. Zachariah, S. Chidangil, M. Valiathan and D. Mathur, Raman tweezers spectroscopy of live, single red and white blood cells, *PLoS One*, 2010, **5**, e10427.

8 C. Ghanashyam, S. Shetty, S. Bharati, S. Chidangil and A. Bankapur, Optical Trapping and Micro-Raman Spectroscopy of Functional Red Blood Cells Using Vortex Beam for Cell Membrane Studies, *Anal. Chem.*, 2021, **93**, 5484–5493.

9 Y.-J. Kim, S. I. Yang and J.-C. Ryu, Cytotoxicity and genotoxicity of nano-silver in mammalian cell lines, *Mol. Cell. Toxicol.*, 2010, **6**, 119–125.

10 R. Foldbjerg, D. A. Dang and H. Autrup, Cytotoxicity and genotoxicity of silver nanoparticles in the human lung cancer cell line, A549, *Arch. Toxicol.*, 2011, **85**, 743–750.

11 L.-C. Cheng, X. Jiang, J. Wang, C. Chen and R.-S. Liu, Nano-bio effects: interaction of nanomaterials with cells, *Nanoscale*, 2013, **5**, 3547–3569.

12 A. Bankapur, S. Barkur, S. Chidangil and D. Mathur, A Micro-Raman Study of Live, Single Red Blood Cells (RBCs) Treated with $AgNO_3$ Nanoparticles, *PLoS One*, 2014, **9**, e103493.

13 M. Kus-Liśkiewicz, P. Fickers and I. Ben Tahar, Biocompatibility and Cytotoxicity of Gold Nanoparticles: Recent Advances in Methodologies and Regulations, *Int. J. Mol. Sci.*, 2021, **22**, 10952.

14 R. Pamies, J. G. H. Cifre, V. F. Espín, M. Collado-González, F. G. D. Baños and J. G. de la Torre, Aggregation behaviour of gold nanoparticles in saline aqueous media, *J. Nanopart. Res.*, 2014, **16**, 2376.

15 A. M. E. Badawy, T. P. Luxton, R. G. Silva, K. G. Scheckel, M. T. Suidan and T. M. Tolaymat, Impact of Environmental Conditions (pH, Ionic Strength, and Electrolyte Type) on the Surface Charge and Aggregation of Silver Nanoparticles Suspensions, *Environ. Sci. Technol.*, 2010, **44**, 1260–1266.

16 A. Habib, M. Tabata and Y. G. Wu, Formation of Gold Nanoparticles by Good's Buffers, *Bull. Chem. Soc. Jpn.*, 2005, **78**, 262–269.

17 J. Xie, J. Y. Lee and D. I. C. Wang, Seedless, Surfactantless, High-Yield Synthesis of Branched Gold Nanocrystals in HEPES Buffer Solution, *Chem. Mater.*, 2007, **19**, 2823–2830.

18 H. Yuan, A. M. Fales, C. G. Khoury, J. Liu and T. Vo-Dinh, Spectral characterization and intracellular detection of Surface-Enhanced Raman Scattering (SERS)-encoded plasmonic gold nanostars, *J. Raman Spectrosc.*, 2013, **44**, 234–239.

19 S. Saverot, X. Geng, W. Leng, P. J. Vikesland, T. Z. Grove and L. R. Bickford, Facile, tunable, and SERS-enhanced HEPES gold nanostars, *RSC Adv.*, 2016, **6**, 29669–29673.

20 R. Garrett and C. Grisham, *Biochemistry*, 2nd ed., Fort Worth, Harcourt College Publishers, 1999, vol. 30, p. 124.

21 W. R. Premasiri, J. C. Lee and L. D. Ziegler, Surface-Enhanced Raman Scattering of Whole Human Blood, Blood Plasma, and Red Blood Cells: Cellular Processes and Bioanalytical Sensing, *J. Phys. Chem. B*, 2012, **116**, 9376–9386.

22 D. Drescher, T. Büchner, D. McNaughton and J. Kneipp, SERS reveals the specific interaction of silver and gold nanoparticles with hemoglobin and red blood cell components, *Phys. Chem. Chem. Phys.*, 2013, **15**, 5364–5373.

23 T. Stepanenko, K. Sofińska, N. Wilkosz, J. Dybas, E. Wiercigroch, K. Bulat, *et al.*, Surface-enhanced Raman scattering (SERS) and tip-enhanced Raman scattering (TERS) in label-free characterization of erythrocyte membranes and extracellular vesicles at the nano-scale and molecular level, *Analyst*, 2024, **149**, 778–788.

24 X.-L. Liu, J.-H. Wang, S. Liang, D.-J. Yang, F. Nan, S.-J. Ding, *et al.*, Tuning Plasmon Resonance of Gold Nanostars for Enhancements of Nonlinear Optical Response and Raman Scattering, *J. Phys. Chem. C*, 2014, **118**, 9659–9664.

25 N. Farkas and J. A. Kramar, Dynamic light scattering distributions by any means, *J. Nanopart. Res.*, 2021, **23**, 120.

26 Y. Li, S. Liu, T. Yao, Z. Sun, Z. Jiang, Y. Huang, *et al.*, Controllable synthesis of gold nanoparticles with ultrasmall size and high monodispersity *via* continuous supplement of precursor, *Dalton Trans.*, 2012, **41**, 11725–11730.

27 W. Xi and A. J. Haes, Elucidation of HEPES Affinity to and Structure on Gold Nanostars, *J. Am. Chem. Soc.*, 2019, **141**, 4034–4042.

28 B. Tang, S. Xu, J. An, B. Zhao, W. Xu and J. R. Lombardi, Kinetic effects of halide ions on the morphological evolution of silver nanoplates, *Phys. Chem. Chem. Phys.*, 2009, **11**, 10286–10292.

29 N. A. Brazhe, E. Y. Parshina, V. V. Khabatova, A. A. Semenova, A. R. Brazhe, A. I. Yusipovich, *et al.*, Tuning SERS for living erythrocytes: Focus on nanoparticle size and plasmon resonance position, *J. Raman Spectrosc.*, 2013, **44**, 686–694.

30 B. Fazio, C. D'Andrea, A. Foti, E. Messina, A. Irrera, M. G. Donato, *et al.*, SERS detection of Biomolecules at Physiological pH *via* aggregation of Gold Nanorods mediated by Optical Forces and Plasmonic Heating, *Sci. Rep.*, 2016, **6**, 26952.

31 F. Bonardi, E. Halza, M. Walko, F. Du Plessis, N. Nouwen, B. L. Feringa, *et al.*, Probing the SecYEG translocation pore size with preproteins conjugated with sizable rigid spherical molecules, *Proc. Natl. Acad. Sci. U. S. A.*, 2011, **108**, 7775–7780.

32 A. Adan, G. Alizada, Y. Kiraz, Y. Baran and A. Nalbant, Flow cytometry: basic principles and applications, *Crit. Rev. Biotechnol.*, 2017, **37**, 163–176.

33 P. Sarmah, C. Ghanashyam, R. Khanna and A. Bankapur, Unraveling biochemical differences in the membrane of functional RBCs and elliptocytes using vortex beam-based micro-Raman spectroscopy, *Spectrochim. Acta, Part A*, 2025, **334**, 125911.

34 J. M. Berg, J. L. Tymoczko, and L. Stryer, *Biochemistry*, 5 ed., New York, W H Freeman, 2002.

35 M. Shylaja and H. Seshadri, Glycoproteins: an overview, *Biochem. Educ.*, 1989, **17**, 170–178.

© 2025 The Author(s). Published by the Royal Society of Chemistry